Efficient Transfer Doping of Carbon Nanotube Forests by MoO_3

Santiago Esconjauregui,[*,†] Lorenzo D'Arsié,[†] Yuzheng Guo,[†] Junwei Yang,[†] Hisashi Sugime,[†] Sabina Caneva,[†] Cinzia Cepek,[‡] and John Robsertson[†]

[†] Department of Engineering, University of Cambridge, CB3 0FA Cambridge, UK
[‡] Istituto Officina dei Materiali – CNR, Laboratorio TASC, I-34149 Trieste, Italy

ABSTRACT

We dope nanotube forests using evaporated MoO_3 and observe the forest resistivity to decrease by two orders of magnitude, reaching values as low as ~5×10^{-5} Ωcm, thus approaching that of copper. Using in-situ photoemission spectroscopy, we determine the minimum necessary MoO_3 thickness to dope a forest and study the underlying doping mechanism. Homogenous coating and tube compaction emerge as key factors for decreasing the forest resistivity. When all nanotubes are fully coated with MoO_3 and packed, conduction channels are created both inside the nanotubes and on the outside oxide layer. This is supported by density functional theory calculations which show a shift of the Fermi energy of the nanotubes and the conversion of the oxide into a layer of metallic character. MoO_3 doping removes the need for chirality control during nanotube growth and represents a step forward towards the use of forests in next-generation electronics and in power cables or conductive polymers.

KEYWORDS: carbon nanotubes, forests, MoO_3, doping, resistivity, interconnects

It has long been predicted that, owing to their extreme current-carrying capacity, carbon nanotube (CNT) forests – and more recently graphene or graphite – are the only known materials suitable to replace copper wiring in future generations of electronics.[1-4] Over recent years, there have been significant advances in the development of CNT-based interconnect technology – especially for vertical interconnects.[5,6] It is now possible to synthesise nanotube forests at microelectronic-compatible conditions (*e.g.* at temperatures below 450 °C), with fine control of nanotube diameter, length, and density (up to 10^{13} CNTs cm^{-2}), and to grow nanotubes on conductive supports and at specific patterned locations.[7-13] However, the design of catalysts able to control nanotube chirality and especially the preferential growth of metallic nanotubes is very challenging.[14-1819] It is particularly difficult to design catalysts and process conditions that can simultaneously give ultra-high area densities, chiral selectivity, and growth on conductive support layers. Unselective growth gives rise to forests with resistivity values up to three orders of magnitude higher than that of Cu.[5,20-21] Thus in an alternative approach, we design the catalyst system to meet the objective of high density and growth on metallic supports, and we dope nanotube forests to achieve the final conductivity. We subsequently observe a dramatic decrease of forest resistivity, achieving values as low as ~5×10^{-5} Ωcm. This value is the lowest resistivity measured to date on a nanotube bundle while keeping the highly ordered alignment. The doping is achieved by evaporation of sub-stoichiometric molybdenum trioxide (denoted herein as MoO_3) on nanotube bundles and systematically evaluated by *in-situ* photoemission spectroscopy. We determine the minimum necessary MoO_3 thickness to dope a forest, and then study the variation of resistivity over various processing conditions. By density functional theory (DFT) calculations, we observe a shift of the Fermi energy of semiconducting nanotubes as well as the conversion of the oxide into a layer of metallic character. We suggest these factors contribute to improving the electrical properties of the forests and thus remove the need for chirality control during CNT growth for application in electronics.

The doping of CNTs has previously been assessed on dispersed nanotubes and on nanotube networks (bucky paper),[22,23] but not yet on aligned forests. When doping an ensemble of nanotubes, the overall resistivity is lowered in two ways: (*i*) the free carrier concentration per nanotube is increased, and (*ii*) the intra-nanotube junction resistance is reduced since carriers are allowed to move more freely between metallic and semiconducting nanotubes. Various materials, other than MoO_3, have been explored to improve the electrical properties of nanotubes. These range from alkali metals and halogens to acidic liquids (*e.g.*

K,[24] I_2,[25] HNO_3,[26] H_2SO_4,[27] and $SOCl_2$) and redox dopants (*e.g.* $FeCl_3$[28] or $AuCl_3$[29]). The selected chemical dictates the doping mechanism (absorption, substitution, or functionalization), the charge transfer, and thus the kind of doping (*n*- or *p*-type), and the doping stability.[30]

MoO_3 is known to strongly and stably *p*-type dope dispersed CNTs, effectively lowering their resistivity. Examples include the fabrication of MoO_3-CNTs bi-layer transparent electrodes, the fabrication of MoO_3-nanodots decorated CNT supercapacitors,[31,32] and the fabrication of CNT-wired MoO_3-nanobelts for lithium storage.[33] More recently, MoO_3 has also been used to *p*-dope graphene (or graphite) and other nanomaterials, and has been envisaged as a key component in transparent electrodes, photocromic and electronic devices, gas sensors, and energy storage systems.[34-40] Since MoO_3 is relatively inexpensive, microelectronic-compatible, and suitable for the large-scale production of devices,[41] this report represents a step forward towards the employment of CNTs in interconnects for next-generation electronics and in applications where copper is to be replaced, including power cables or conductive polymer fibres.

RESULTS AND DISCUSSION

Doping nanotube forests with MoO_3 allows us to dramatically decrease the forest resistivity by up to two orders of magnitude. The average measured value after doping is ~5×10^{-5} Ωcm. To extract the resistivity, we use an approach that includes nanotube growth, placement of a bundle of nanotubes on a flat surface, evaporation of MoO_3, and bundle compaction (Figure 1a). We first grow forests with heights of either two or four millimetres. The nanotubes are a mix of single- and double-walled with diameters ranging between ~1.5 - 2.5 nm. Various chiralities are expected. Then, by employing ultra-fine, straight pointed precision tip tweezers, we pull out bundles of nanotubes from the forests and place them (lying horizontally) onto a SiO_2 support (Figure 1b). The nanotubes lie unpacked but maintain their longitudinal alignment and exhibit large spacing between neighbouring tubes or bundles (in the order of tens of nanometres). Note that the final curly shape of the bundles (as seen in Figure 1b) is related to the extremely high aspect ratio of the nanotubes and the processing steps, other than nanotube structural defects. Raman analysis shows a D/G ratio of ~0.7, typical of double-walled CNTs (not shown here). Subsequently, we fix one of the extremes of the bundles and then evaporate nominally 3 to 5 nm of MoO_3. To ensure the coating is as homogenous as possible, we vary the bundle position during the evaporation, so that the oxide reaches the nanotubes from various angles. Since the nanotubes are unpacked, the evaporated oxide reaches both outermost and innermost nanotubes. After evaporation, the fixing is removed and the nanotubes are soaked with isopropyl alcohol (IPA), causing a compaction of the nanotubes.[42,43] Since the solubility of MoO_3 in IPA is negligible, the oxide coating is not removed or damaged. When the IPA evaporates, the nanotubes become nearly fully compacted, as assessed by SEM analysis (250k magnification), Figure 1c. The spacing between neighbouring tubes (or bundles) is reduced to <5 nm. We also determine that the Herman's orientation factor[44] is above 0.82, thus the bundles after compaction exhibit a high degree of alignment. No materials, other than MoO_3, appear to coat the nanotube surface. The cross section is determined by both SEM and AFM analysis. For comparison, we show the compaction of pristine nanotubes also used for resistivity assessment (Figure 1d). The area density of the forests after compaction is estimated to be 5-8$\times10^{12}$ CNTs cm^{-2} for both cases.

A four-probe set up (as indicated in Figure 1b) is used to measure the electrical resistivity of the doped forests. Electrical probing is done along the *z* axis of the nanotubes, *i.e.* between tip and bottom areas of the bundles. Prior to MoO_3 evaporation, compacted

bundles systematically show a resistivity averaging $8\pm0.6\times10^{-3}$ Ωcm. After evaporation and compaction, the resistivity is observed to decrease by about two orders of magnitude. Over more than twenty assessments, we measure values averaging $5\pm0.8\times10^{-5}$ Ωcm; the lowest value we obtain is 1.3×10^{-5} Ωcm. In comparison to pristine forests, the dispersion is slightly larger, and we have actually discarded bundles whose measurements are well outside the 3σ of the average (2 out of 24 measurements). The average resistivity value of $5\pm0.8\times10^{-5}$ Ωcm represents one the lowest measured for an ensemble of nanotubes with a highly ordered structure (whether on blanket supports or in patterned architectures). It is lower than that of graphite (~10^{-4} Ωcm)[45] and approaches that of copper (~10^{-6} Ωcm).[46] This is summarised in Table 1. We hypothesize the after-doping resistivity could be even lower if the pristine bundles consisted only of ideal, defect-free nanotubes.

A second set of experiments allows us to confirm the change in the electrical properties of the nanotubes. By employing a two-probe set up, we observe a decrease in the overall forest resistance of doped nanotubes, compared to pristine ones, as shown Figure 2. For these experiments, we grow forests with a gradient of heights, ranging between ~100 and ~800 μm, and depth of 250 μm, Figure 3a. This nanotube pattern allows the evaluation of the resistance of nanotubes with different lengths, while keeping the other nanotube properties constant for all measurements. Prior to evaporation, we place the forests horizontally onto a SiO_2 support and probe the nanotubes longitudinally between tip and bottom areas. The overall electrical resistance of pristine forests is 331±21, 785±42, and 1066±70 Ω (for nanotube lengths of 200, 500, and 800 μm respectively). After unidirectional evaporation of 3 to 5 nm MoO_3, we perform the same measurements starting from the topmost surface of the nanotubes. We observe resistance values of 22±2, 45±5, and 92±11 Ω respectively, thus averaging up to one order of magnitude lower. For comparison, the sheet resistance of continuous MoO_3 films evaporated on SiO_2 is orders of magnitude higher. Although the measurements after evaporation are reproducible, we observe greater dispersion of the resistance values depending on how much the needle probe is pressed. When the probe needle is purposely pushed deeper into the nanotubes, the resistance values lie between those obtained for doped and pristine forests. Since we have not induced CNT compaction in these experiments, the nanotubes do not behave as a solid material, but as individual conductors, and therefore the electrical measurements depend on the number and type of nanotubes contacted. These results suggest the presence of a MoO_3 concentration gradient and thus the probing of nanotubes un-coated by the oxide. The highest concentration of MoO_3 is expected

at the topmost surface (where the evaporated species first impinge), and then gradually to decrease towards the inner areas of the forest, as schematically depicted in Figure 3b. The drop in resistance values thus confirms the nanotubes have been effectively improved their electrical properties, in agreement with results shown in Figure 1 and Table 1. The dispersion of values, instead, indicates a MoO_3 concentration gradient. Figure 3c compares the nanotube alignment and spacing for the pristine state and after MoO_3 evaporation.

In a third set of experiments, we evaluate the effect of compaction. Negligible changes of resistivity are determined for un-compacted bundles. To determine this, we devise forest architectures contacting two metallic electrodes. Using e-beam lithography, we first pattern Al_2O_3/Fe (10/0.5 nm) on a SiO_2 support. The samples are then exposed to optimised annealing and growth conditions, leading to patterned forests with predefined areas. The height is varied between 300 and 500 μm (Figure 4a). After growth, we flip the forests using IPA, and by further e-beam lithography and evaporation, we define (Cr/Au: 5:50 nm) electrodes at each end, Figure 4b. We evaporate nominally 3 to 5 nm of MoO_3 and probe the structures prior and after doping, using a two-probe set up. The values average $5\pm0.8\times10^{-3}$ Ωcm for pristine forests and remain practically unchanged after electrode fabrication and evaporation. The best value of $\sim2\times10^{-3}$ Ωcm does not reflect any doping-related improvement. High-magnification SEM inspections show the absence of any residues on the nanotubes, but in comparison with our previous doped forests, the nanotubes (or bundles) appear to be of much lower area densities (Figure 4c; compare to Figure 1c). The average distance between two nanotubes or bundles is now 20 to 50 nm. We also note that if the nanotubes are cross-contaminated with the lithography materials used for electrode definition, the doping might have been affected (*i.e.* the oxide could not be in direct contact with the nanotubes). Altogether, these results are extremely useful for designing a manufacturing set up for successful doping of forests.

Additionally, we perform *in-situ* X-ray and ultra violet photoemission spectroscopy (XPS and UPS) during the evaporation of MoO_3. Figure 5a details the evolution of the work function of the forests as a function of the evaporated thickness of MoO_3. For this, we measure the Fermi level and the secondary photon electron cut-off by UPS applying a negative bias of ~9 eV. Initially, the work function has a value of 4.40 eV (corresponding to pristine nanotubes) and gradually increases with the thickness of evaporated MoO_3. For 0.5, 0.75, and 1 nm, we measure 4.95, 5.16, and 5.24 eV respectively. The saturation value is ~5.40 eV. For reference, the measurement for the oxide on bare Si/SiO_2 is 5.98 eV. The

doping is also determined by XPS measurements, Figure 5(b-d). Figure 5b shows the evolution of the C 1*s* core level for the entire thickness of evaporated MoO_3. The maxima is centred at ~284.5 eV and shifts towards lower binding energies as we evaporate MoO_3, suggesting a C-Mo interaction. The intensity gradually decreases which is related to the increasing thickness of the oxide. This is clearly seen when fitting the raw data. The C 1*s* core level spectrum of pristine nanotubes presents four main components, Figure 5c. They can be associated to C-C sp^2, C-C sp^3, C-O, and C=O, respectively centred at 284.4, 285.8, 286.8, and 288.7 eV. The sp^2 component is attributed to graphene walls. The presence of a weak sp^3 component, instead, can arise from wall defects and/or deleterious carbon absorbed on air exposure during transport. These features are also present in the C 1*s* spectrum after the evaporation of 2 nm of MoO_3 -the doping saturation thickness (Figure 5d). However, we observe two main changes: (*i*) the appearance of an extra component at ~283.3 eV which is related to the C-Mo interaction and (*ii*) a shift of ~0.10 eV on the C-C sp^2 and C-C sp^3 components towards lower binding energies. Given that all photoemission spectra are aligned to the Fermi level, the shift can be attributed to a *p*-type doping of the nanotubes.

The effect of the doping is summarised in Figure 5e. The work function of the forests increases with increasing thickness of the evaporated MoO_3. Up to a nominal thickness of 1 nm of MoO_3, the shift appears to be very sharp, about 0.8 eV. Following further evaporation, it is more gradual and, at a nominal thickness of 2 nm MoO_3, the shift saturates. Increased thicknesses (up to 4 nm) do not produce further shifts. Similarly, the shift of the band bending is correlated to the evaporated thickness of MoO_3. In this case, however, the maximum shift is ~0.1 eV and the saturation is reached after evaporating ~0.5 nm of MoO_3. As a result, the interface dipole (after reaching saturation at nominal 2 nm MoO_3) is calculated to be 0.90 eV. This behaviour is in agreement with that observed on MoO_3-doped graphene,[37] and confirms an electron transfer from the nanotube surface towards the thin MoO_3 film and, hence, the *p*-type doping of the forests.

The effective *p*-type doping of CNTs stems from a favourable energy level alignment between the nanotubes and the oxide. The large work function difference between MoO_3 (~6.8 eV) and CNTs (typically of ~4 eV) drives a spontaneous electron transfer from the CNTs towards MoO_3, and hence the formation of a large interface dipole and band-bending to align the Fermi level of the nanotubes to the charge neutrality level of the MoO_3. This gives rise to a hole accumulation layer in the CNTs and thus to an effective hole doping, *i.e.* *p*-type doping. The large work function of MoO_3 arises from the fact that MoO_3 exhibits a closed shell character and is a layered material.[47] Owing to their large Mo-to-O

stoichiometry, the layers have terminal oxygen on the outside (anionic sites), but they are overall neutral. This particular Mo-O arrangement creates an additional dipole layer that lowers the electrostatic potential of the inner Mo-O units, giving rise to the high work function, which in turn causes the *p*-type doping of the forests.

Using DFT calculations, we assess the atomic and electronic structure of various MoO_3-doped single-walled CNTs. We test various ideal, defect-free semiconducting and metallic nanotubes as a model system, among which (7,0), (4,2), (11,0), (6,3), and (9,3). The band structure for (11,0) is shown in Figure 6a. In the pristine case, the band gap is of 0.7 eV and disappears after MoO_3 doping (Figure 6b). The Fermi level in MoO_3 is pinned in the valence band, indicating the charge transfer between MoO_3 and the CNTs. Figure 6c shows an increase in Mo atoms up to achieving the equivalent of ~2 nm of evaporated MoO_3. The ratio between C atoms and Mo atoms is close to 3:1. We note that increasing the number of Mo atoms also gives rise to a change in the nanotube symmetry, which might also contribute to improve nanotube conductivity.[48] Similar effects are observed on the other semiconducting nanotubes. On the other hand, when MoO_3 interacts with metallic-type nanotubes there are no changes in their band gap, but the Fermi level of the oxide is also pinned in the valence band and the symmetry is lost. The charge transfer for metallic nanotubes is thus in agreement with previous experimental work showing no evidences of nanotube doping selectivity for diameter or chirality.[49] Statistically, in a typical forest of single-walled or small diameter nanotubes, only a third is involved in conduction (*i.e.* the metallic-type CNTs). As shown by DFT calculations, a MoO_3-doped forest should consist of *metallic-like* nanotubes only, so that all of them contribute to conduction. In their pioneer work of doping CNTs with MoO_3, Hellstrom *et al.*[23] suggested that the number of free carrier concentration per nanotube is dramatically increased. This was experimentally evidenced by the suppression of van Hove transitions, which is consistent with a charge transfer and also with the conversion of semiconducting nanotubes into metallic ones. In agreement with the DFT calculations, the charge transfer appears as the major contribution to improve the resistivity of a nanotube forest. The calculations also show the creation of channels for conduction on the oxide layer which might also contribute to decreasing the resistivity. This is cartooned in Figure 6d.

Two factors emerge to be critical for the charge transfer to take place and hence to decrease the resistivity of a nanotube forest by MoO_3 doping. First, *ideally* each nanotube has to be homogeneously coated across its whole surface. Second, the ensemble of nanotubes must be fully compacted (after MoO_3 doping) as this configuration appears to maximise the charge transfer between nanotubes. Unlike doping layered materials (*e.g.* graphene) or low-

density entangled nanotubes (*e.g.* bucky paper), both requirements are challenging to fully achieve on forests. In evaporating MoO_3, the whole length of the nanotubes is relatively easy to reach, whereas the whole external area is more difficult to coat. Since the evaporation process is unidirectional, the doping species impinge on the exposed area of the nanotubes only. In addition, the nanotubes themselves can produce a shadow effect, such that the innermost nanotubes of the forests may remain in a pristine state, (*i.e.* a MoO_3 concentration gradient is created, as depicted in Figure 3b). Another important factor is the area density of the forests: the higher the nanotube packing, the more restricted the access for the dopant species. These facts must be taken into account when devising a scalable doping process for industrial applications.

Finally, we note there exists today a large number of chemical strategies to change the electronic properties of nanotubes, but unlike MoO_3, each material appears to present some drawbacks for industrial applications. For instance, alkali metals and acids have proved a strong doping effect but both types of materials are not fully compatible with microelectronics processing. A similar problem rises with halogens. The doping effect is very strong but it easily becomes unstable at the operating temperatures of electronic devices. It is for these reasons that MoO_3 emerges as one of the most suitable materials for doping nanotube forests. MoO_3 is compatible with microelectronics processing and can be deposited by evaporation or by spinning of a MoO_3-containing solution. This strengthens the potential use of MoO_3 doping not only for nanotube-based interconnects in electronics, but also for power cables or conductive polymer fibres.

CONCLUSION

In conclusion, by using evaporated films of MoO_3, we demonstrate *p*-type doping of nanotube forests while keeping their highly ordered vertical alignment. We establish that a nominal thickness of ~2 nm ensures the required electron transfer for improving the resistivity of the nanotubes by two orders of magnitude, reaching values of $\sim 5\times10^{-5}$ Ωcm and thus approaching the resistivity of copper. Such a result removes the need for synthesising nanotubes with controlled chirality for certain applications (*e.g.* interconnects). In order to maximise the charge transfer between the nanotubes and the oxide, all nanotubes have to be homogeneously coated and fully compacted. Given that MoO_3 is relatively inexpensive and

microelectronic-compatible, MoO_3–doped forests could find applications in future generation electronics, as well as in other applications requiring highly conductive materials (*e.g.* power cables or conductive polymer fibres).

MATERIALS AND METHOD

We use as substrate Si(100) coated with 300 nm of SiO_2 on which we thermally evaporate a nominal 0.5 nm of Fe (base pressure is ~10^{-6} mbar). After deposition the samples are transferred in air to a hot-wall CVD furnace and heated at a rate of 50 ºC min^{-1} up to the desired growth temperature (700 and 750 ºC) in 1 bar of Ar:H_2 (1000:500 sccm). Once the growth temperature is achieved, we wait for 5 min and then add 3 or 10 sccm of C_2H_2 for 15 min. After growth, the system is cooled down in Ar until reaching room temperature (RT). The nanotubes are characterised by scanning electron microscopy (SEM) and transmission electron microscopy (TEM). The area density of the forests is derived by the weight gain method.[12]

In order to determine the thickness of MoO_3 required to saturate the doping of a forest, we use *in-situ* photoemission spectroscopy during MoO_3 evaporation. We perform X-ray photoemission spectroscopy (XPS) using an Mg X-ray source ($h\nu \approx 1253.6$ eV) and UV photoemission spectroscopy (UPS) with a Helium lamp (He I, $h\nu \approx 21.2$ eV) in normal emission geometry. We detect electrons with a hemispherical sector electron energy analyzer with an overall energy resolution of ~0.8 eV for XPS and ~0.1 eV for UPS. For these measurements, we evaporate MoO_3 *in situ*, at a pressure of ~10^{-9} mbar. The photoelectron binding energy is referenced to the Fermi edge. The spectra are normalized to the incident photon flux and have been analyzed by performing a nonlinear mean square fit of the data following the Levenberg-Marquardt algorithm. We use a Shirley background and reproduce the photoemission intensity by using asymmetric Doniach-Sunjic functions convoluted with Gaussian profiles. The value of the work function as a function of doping is determined by measuring *via* UPS the Fermi level and the secondary photoelectrons cut-off.[50] The measurements are taken in normal emission geometry, by applying a negative bias of ~9V, which allows the acceleration of the lowest energy secondary electrons into the spectrometer.

We study the doping of nanotubes by DFT calculations. We use CASTEP code with an ultra-soft pseudo-potential and the PBE-style generalised gradient approximation. A 2 nm vacuum layer is inserted between neighbouring CNTs to eliminate the image interaction induced by a periodical boundary condition in the plane-wave method. We first focus on the semiconducting nanotubes, as they statistically can represent up to ~66% of an ensemble of nanotubes. For MoO_3, we have simulated various termination cases with different ratio of O

occupation. Both amorphous and crystalline MoO_3 have been used, and both give similar doping effects. All atomic structures are relaxed with a residual force of 0.02 eVÅ^{-1}. We test various semiconducting and metallic nanotubes, among which (7,0), (4,2), (11,0), (6,3), and (9,3).

Current-voltage (I-V) measurements are performed using a two- or four-terminal Cascade Probe stations set with a low bias condition ($|V| < 0.05$ V) during all measurements (in order to avoid heating effects). All measurements are performed at RT. The total resistance of the samples is determined from the slopes of a least squares fit to I-V response. In all cases, the measurements are carried out prior to and after doping. To derive the values of resistivity, we assess the cross-sectional area of each characterised bundle by both SEM and AFM analysis, after IPA-induced compaction. Despite the compaction, the bundles are not fully close-packed, and hence, cross-sectional areas also include the inter-tube space (<5 nm). We evaluate 12 pristine bundles and 24 different bundles after doping.

ACKNOWLEDGEMENT

The authors acknowledge financial support from European project Grafol.

Figure 1. (a) Schematic of techniques employed for nanotube forest doping. (b) Optical image of nanotubes peeled off from a forest and compacted for electrical characterisation. (c-d) Compacted forests after MoO_3 doping and pristine state respectively.

Figure 2. Resistance for doped and pristine nanotubes as a function of different forest length. The dash-type line shows resistance values obtained when probing both doped and un-doped tubes.

Figure 3. (a) SEM image of gradient-height forests. (b) Schematic for MoO_3 evaporation in one direction. (c) SEM image of a nanotube bundle prior to and after doping.

Figure 4. (a) Patterned nanotube forests on SiO_2 substrate. (b) Optical image of a forest after flipping and electrode definition. (c) SEM image showing the nanotubes after evaporation; the nanotubes appear to exhibit very low compaction.

Figure 5. Variation of the secondary cut-off in UPS spectra, related to the shift of the forest work function. (b) XPS spectra of the C 1*s* aligned to the Fermi energy. (c-d) C 1*s* core level spectra before and after the evaporation of 2 nm MoO_3. (e) Comparison of work function shift and band bending for different thicknesses of evaporated MoO_3.

Figure 6. (a-b) DFT-calculated Fermi energy for a semiconducting (10,0) nanotube in pristine and doped states. (c) Change of nanotube symmetry with increased MoO_3 concentration. (d) Model of MoO_3-doped forests: Hole accumulation on the nanotube side induces *p*-type doping, while the oxide side becomes metallic.

Table 1. Comparison of resistivity for various material systems.

Figure 1

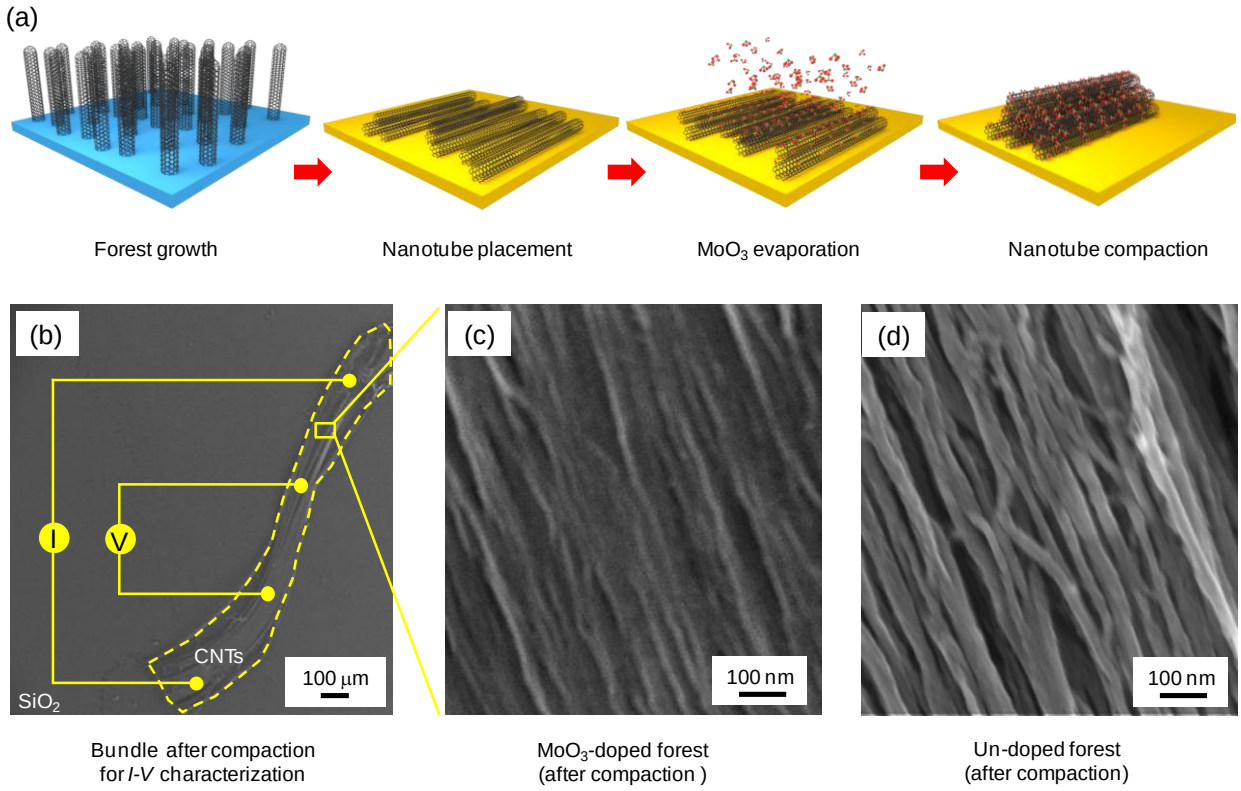
(a)
Forest growth
Nanotube placement
MoO_3 evaporation
Nanotube compaction
(b)
I
V
CNTs
100 μm
SiO_2
Bundle after compaction
for *I-V* characterization
(c)
100 nm
MoO_3-doped forest
(after compaction)
(d)
100 nm
Un-doped forest
(after compaction)

Figure 2.

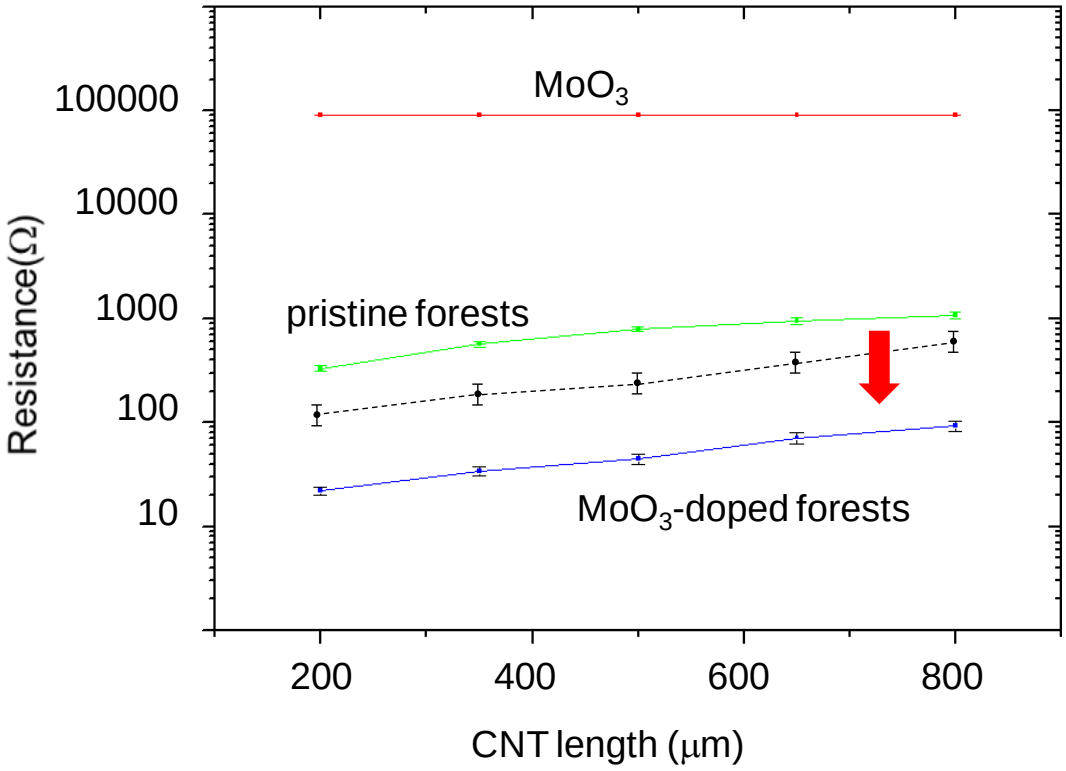
MoO3
pristine forests
MoO3-doped forests
Resistance(Ω)
100000
10000
1000
100
10
200
400
600
800
CNT length (μm)

Figure 3.

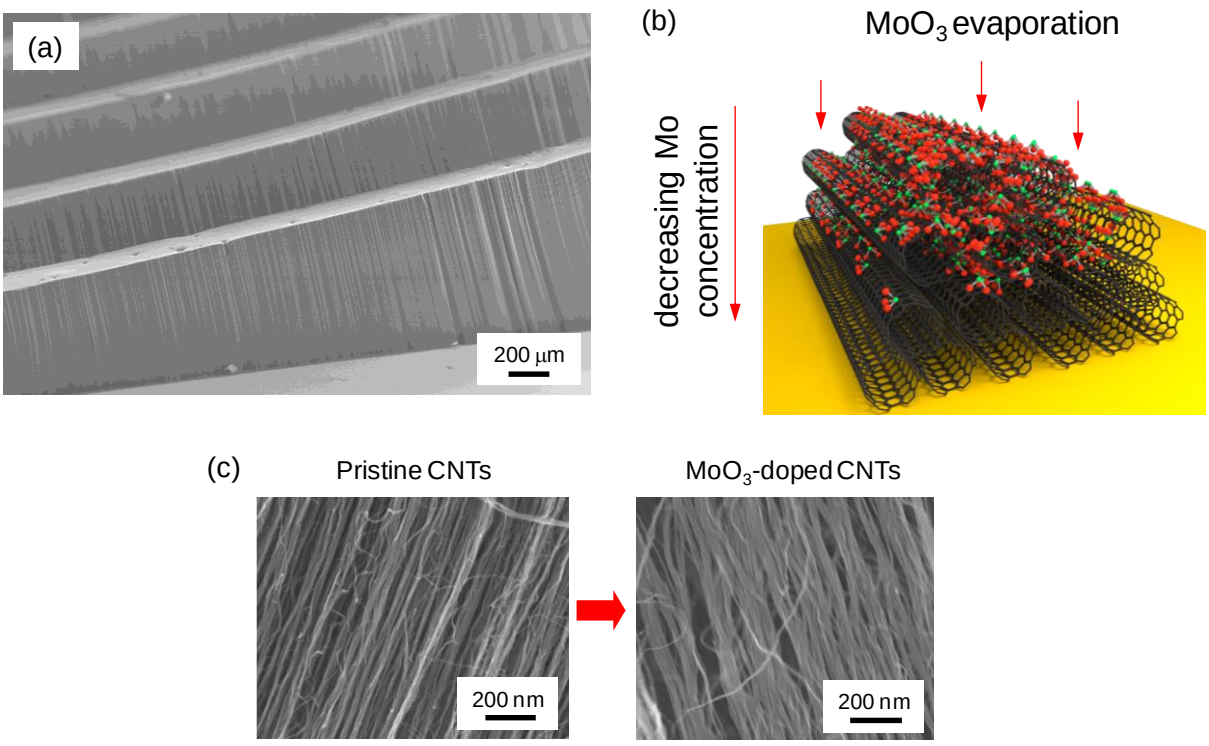
(a)
200 μm
(b)
MoO3 evaporation
decreasing Mo concentration
(c)
Pristine CNTs
MoO3-doped CNTs
200 nm
200 nm

Figure 4.

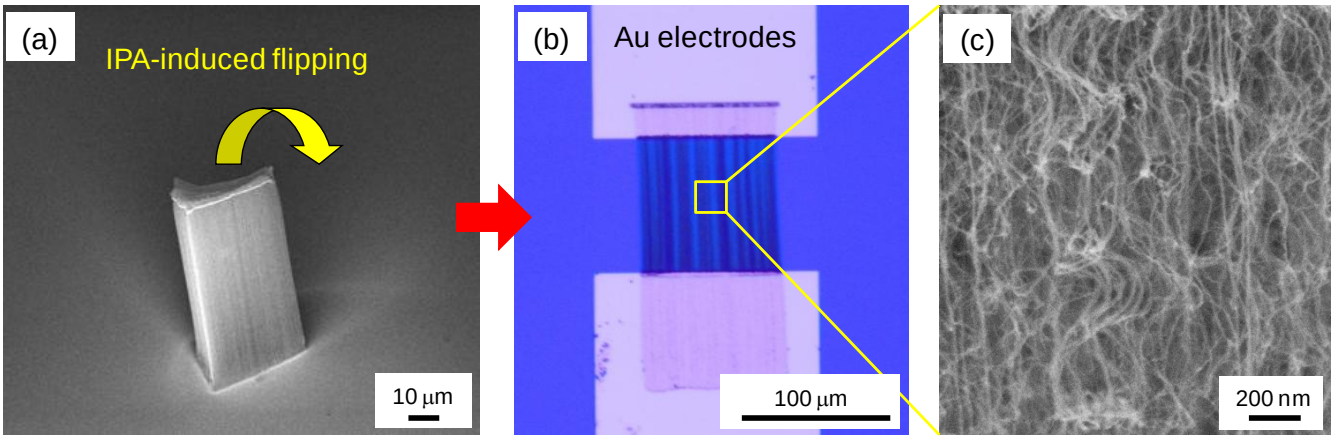

Figure 5.

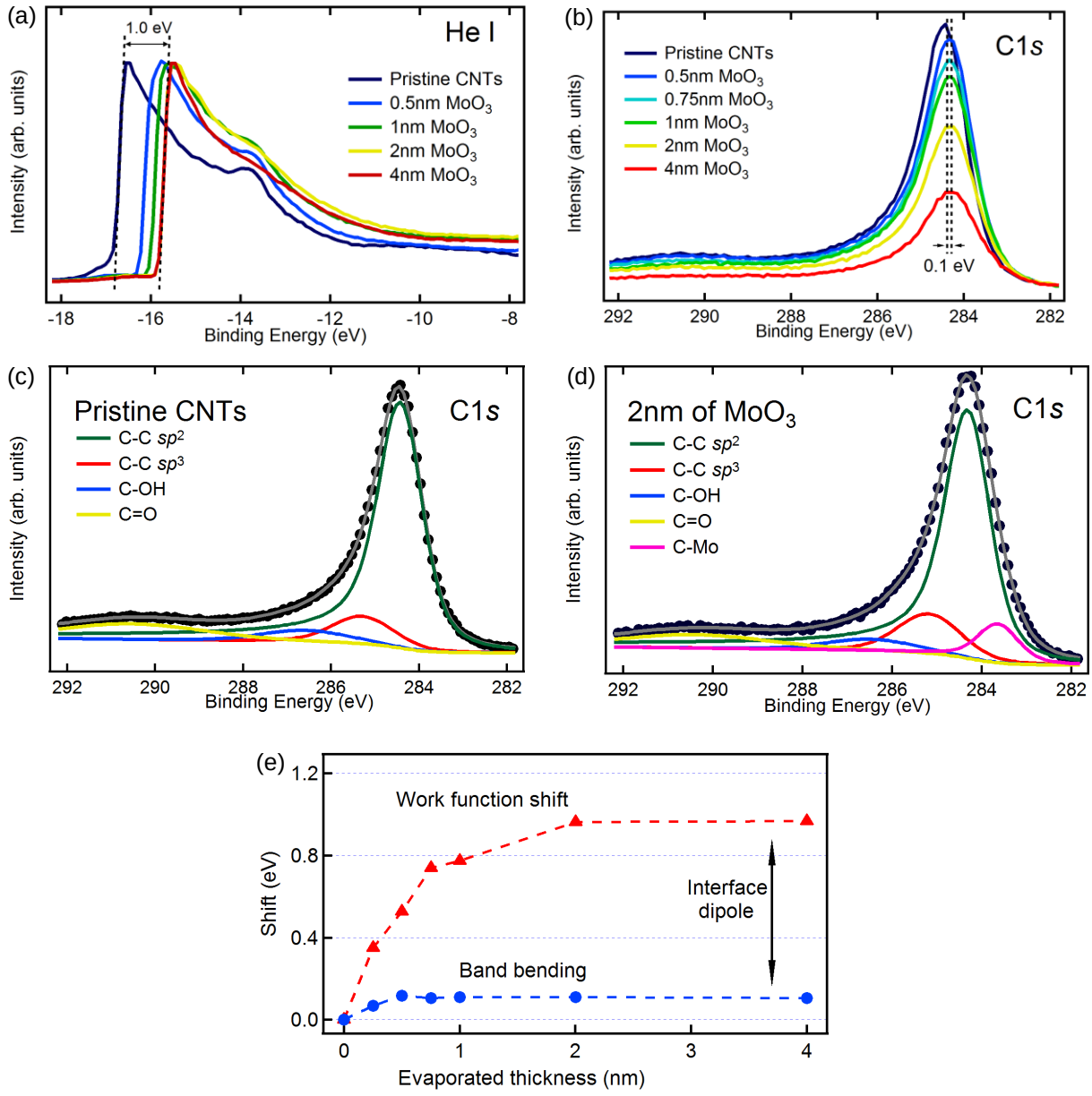
(a)
1.0 eV
He I
Pristine CNTs
0.5nm MoO3
1nm MoO3
2nm MoO3
4nm MoO3
Intensity (arb. units)
-18
-16
-14
-12
-10
-8
Binding Energy (eV)
(b)
C1s
Pristine CNTs
0.5nm MoO3
0.75nm MoO3
1nm MoO3
2nm MoO3
4nm MoO3
0.1 eV
Intensity (arb. units)
292
290
288
286
284
282
Binding Energy (eV)
(c)
Pristine CNTs
C1s
C-C sp2
C-C sp3
C-OH
C=O
Intensity (arb. units)
292
290
288
286
284
282
Binding Energy (eV)
(d)
2nm of MoO3
C1s
C-C sp2
C-C sp3
C-OH
C=O
C-Mo
Intensity (arb. units)
292
290
288
286
284
282
Binding Energy (eV)
(e)
Work function shift
Interface dipole
Band bending
Shift (eV)
1.2
0.8
0.4
0.0
0
1
2
3
4
Evaporated thickness (nm)

Figure 6.

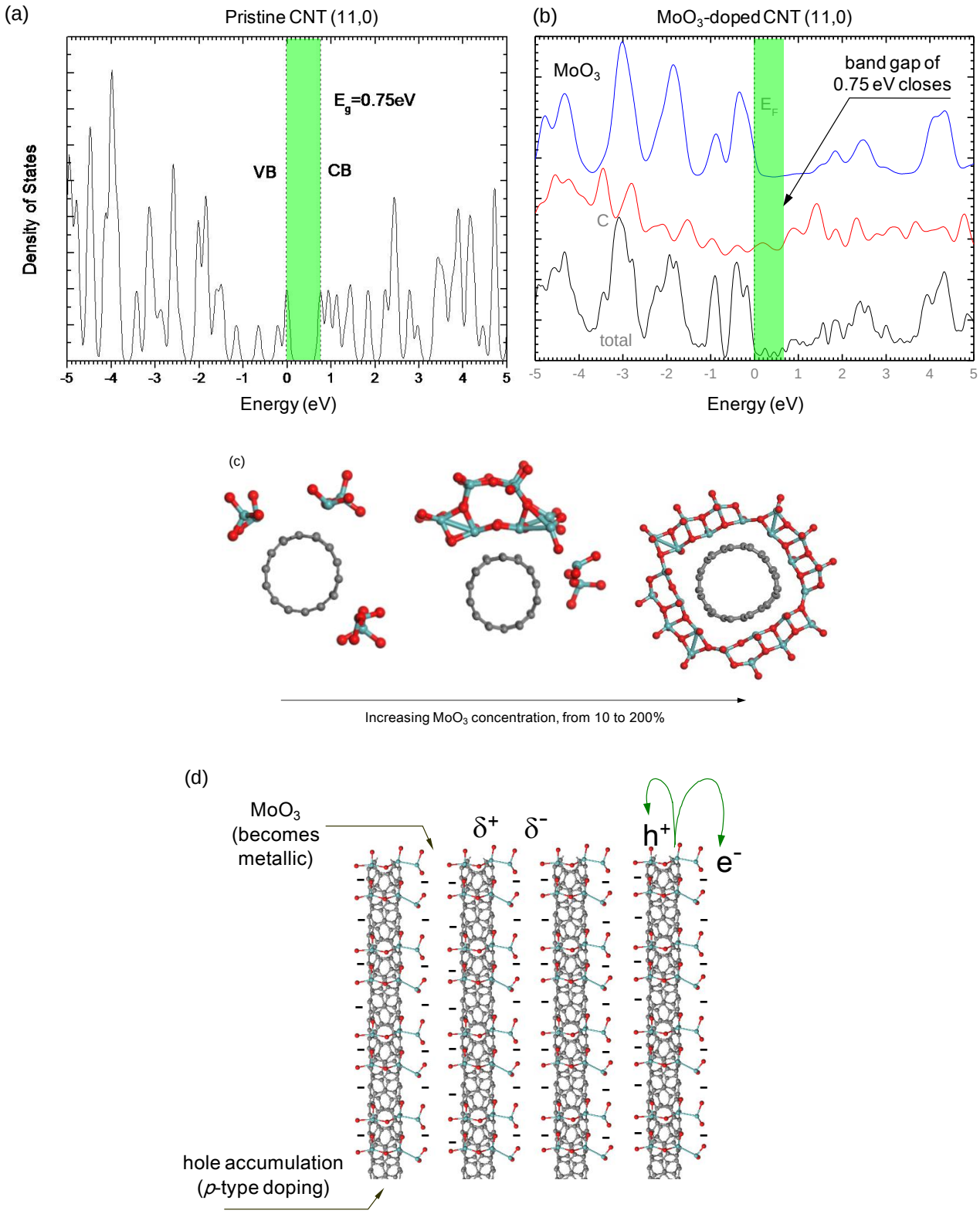
(a)
Pristine CNT (11,0)
Density of States
E_g=0.75eV
VB
CB
Energy (eV)
(b)
MoO_3-doped CNT (11,0)
MoO_3
band gap of
0.75 eV closes
E_F
C
total
Energy (eV)
(c)
Increasing MoO_3 concentration, from 10 to 200%
(d)
MoO_3
(becomes
metallic)
δ^+
δ^-
h^+
e^-
hole accumulation
(*p*-type doping)

Table 1.

Material System	Resistivity (Ωcm)	Reference
MoO_3-doped forests	1.3×10^{-5}	this work
Pristine forests	8.1×10^{-3}	this work
Patterned CNTs	3.7×10^{-3}	Chiodarelli *et al*.
Bulk CNTs + H_2SO_4	1.1×10^{-3}	Zhou *et al*.
Graphite	3.6×10^{-3}	Krishnan *et al*.
Copper	1.6×10^{-6}	Cho *et al*.

REFERENCES

1 Avouris, P.; Chen, J. Nanotube Electronics and Optoelectronics. *Mater. Today* 2006, 9, 46-54.

2 Katagiri, M.; Sakuma, N.; Suzuki, M.; Sakai, T.; Sato, S.; Hyakushima, T.; Nihei, M.; Awano, Y. Carbon Nanotube Vias Fabricated by Remote Plasma-Enhanced Chemical Vapor Deposition. *Jpn. J. Appl. Phys.* 2008, 47, 2024-2027.

3 Awano, Y.; Sato, S.; Nihei, M.; Sakai, T.; Ohno, Y.; Mizutani, T. Carbon Nanotubes for VLSI: Interconnect and Transistor Applications. *P. IEEE* 2010, 98, 2015-2031.

4 Robertson, J.; Zhong, G. F.; Esconjauregui, C. S.; Bayer, B. C.; Zhang, C.; Fouquet, M.; Hofmann, S. Applications of Carbon Nanotubes Grown by Chemical Vapor Deposition. *Jpn. J. Appl. Phys.* 2012, 51, 8.

5 Robertson, J.; Zhong, G.; Hofmann, S.; Bayer, B. C.; Esconjauregui, C. S.; Telg, H.; Thomsen, C. Use of Carbon Nanotubes for VLSI Interconnects. *Diam. Relat. Mater.* 2009, 18, 957-962.

6 Nihei, M.; Horibe, M.; Kawabata, A.; Awano, Y. Simultaneous Formation of Multiwall Carbon Nanotubes and Their End-Bonded Ohmic Contacts to Ti Electrodes for Future ULSI Interconnects. *Jpn. J. Appl. Phys.* 1 2004, 43, 1856-1859.jj

7 Hata, K.; Futaba, D. N.; Mizuno, K.; Namai, T.; Yumura, M.; Iijima, S. Water-Assisted Highly Efficient Synthesis of Impurity-Free Single-Walled Carbon Nanotubes. *Science* 2004, 306, 1362-1364.

8 Li, X.; Cao, A.; Jung, Y. J.; Vajtai, R.; Ajayan, P. M. Bottom-Up Growth of Carbon Nanotube Multilayers: Unprecedented Growth. *Nano Lett.* 2005, 5, 1997-2000.

9 Yamada, T.; Maigne, A.; Yudasaka, M.; Mizuno, K.; Futaba, D. N.; Yumura, M.; Iijima, S.; Hata, K. Revealing the Secret of Water-Assisted Carbon Nanotube Synthesis by Microscopic Observation of the Interaction of Water on the Catalysts *Nano Lett*. 2008, 8, 4288–4292

10 Esconjauregui, S.; Fouquet, M.; Bayer, B. C.; Ducati, C.; Smajda, R.; Hofmann, S.; Robertson J. Growth of Ultra-High Density Vertically-Aligned Carbon Nanotube Forests for Interconnects. *ACS Nano* 2010, 4, 7431-7436.

11 Zhong, G.; Warner, J. H.; Fouquet, M.; Robertson, A. W.; Chen, B.; Robertson, J. Growth of Ultrahigh Density Single-Walled Carbon Nanotube Forests by Improved Catalyst Design. *ACS Nano* 2012, 6, 2893-2903.

12 Esconjauregui, S.; Xie, R.; Fouquet, M.; Cartwright, R.; Hardeman, D.; Yang, J.; Robertson, J. Measurement of Area Density of Vertically Aligned Carbon Nanotube Forests by the Weight-Gain Method. *J. Appl. Phys*. 113, 144309 (2013).
13 Sugime, H.; Esconjauregui, S.; D'Arsié, L.; Yang, J.; Makaryan, T.; Robertson, J. Growth Kinetics and Growth Mechanism of Ultrahigh Mass Density Carbon Nanotube Forests on Conductive Ti/Cu Supports. *ACS Appl. Mater. Interfaces.* 6, 15440-15447 (2014).
14 Harutyunyan, A. R.; Chen, G.; Paronyan, T. M.; Pigos, E. M.; Kuznetsov, O. A.; Hewaparakrama, K.; Kim, S. M.; Zakharov, D.; Stach, E. A.; Sumanasekera, G. U. Preferential Growth of Single-Walled Carbon Nanotubes with Metallic Conductivity. *Science* 2009, 326, 116-120.
15 Koziol, K. K. K.; Ducati, C.; Windle, A. H.Carbon Nanotubes with Catalyst Controlled Chiral Angle. Chem. Mat. 22, 4904–4911 (2010).
16 Sundaram, R. M.; Koziol, K. K. K.; Windle, A. H. Continuous Direct Spinning of Fibers of Single-Walled Carbon Nanotubes with Metallic Chirality. Adv. Mat. 23, 5064–5068 (2011).
17 Sanchez-Valencia, J.; Dienel, T.; Gröning, O.; Shorubalko, I.; Mueller, A.; Jansen, M.; Amsharov, K.; Ruffieux, P.; Fasel, R. Controlled Synthesis of Single-Chirality Carbon Nanotubes. *Nature* 512, 61–64 (2014).
18 Yang, F.; Wang, X.; Zhang, D.; Yang, J.; Luo, D.; Xu, Z.; Wei, J.; Jian-Qiang, W.; Xu, Z. Peng, F. *et al*. Chirality-Specific Growth of Single-Walled Carbon Nanotubes on Solid Alloy Catalysts. *Nature* 510, 522–524 (2014).
19 Hersam, M. Progress Towards Monodisperse Single-Walled Carbon Nanotubes. *Nat. Nanotechnol*. 3, 387-394 (2008).
20 Yokoyama, D.; Iwasaki, T.; Ishimaru K.; Sato, S.; Hyakushima, T.; Nihei, M.; Awano, Y.; Kawarada, H. Electrical Properties of Carbon Nanotubes Grown at a Low Temperature for Use as Interconnects. *Jap. J. Appl. Phys*. 47, 1985-1990 (2008).
21 Chiodarelli, N.; Masahito, S.; Kashiwagi, Y.; Li, Y.; Arstila, K.; Richard, O.; Cott, D. J.; Heyns, M.; Gendt, S. D.; Groeseneken, G. *et al*. Measuring the Electrical Resistivity and Contact Resistance of Vertical Carbon Nanotube Bundles for Application as Interconnects. *Nanotechnology* 22, 085302 (2011).
22 Dettlaff-Weglikowska, U.; Skákalová, V.; Graupner, R.; Jhang, S H.; Kim, B H.; Lee, H J.; Ley, L.; Park, Y W.; Berber, S.; Tománek, D.; Roth, S. Effect of $SOCl_2$ Treatment on

Electrical and Mechanical Properties of Single-Wall Carbon Nanotube Networks. *J. Am. Chem. Soc*. 127, 5125–5131 (2005).

23 Hellstrom, S. L.; Vosgueritchian, M.; Stoltenberg, R. M.; Irfan, I.; Hammock, M.; Wang, Y. B.; Jia, C.; Guo, X.; Gao, Y.; Bao, Z. Strong and Stable Doping of Carbon Nanotubes and Graphene by MoOx for Transparent Electrodes. *Nano Lett*. 12, 3574–3580 (2012).

24 Lee, R. S.; Kim, H. J.; Fischer, J. E.; Thess, A.; Smalley R. E. Conductivity Enhancement in Single-Walled Carbon Nanotube Bundles Doped with K and Br. *Nature* 388, 255 (1997).

25 Zhao,Y.; Wei, J.; Vajtai, R.; Ajayan, P. M.; Barrera, E. V. Iodine Doped Carbon Nanotube Cables Exceeding Specific Electrical Conductivity of Metals. *Scientific Reports* 1, 83 (2011).

26 Graupner, R.; Abraham, J.; Vencelová, A.; Seyller, T.; Hennrich, F.; Kappes, M. M.; Hirsch, A.; Ley, L. Doping of Single-Walled Carbon Nanotube Bundles by Brønsted Acids. *Phys. Chem. Chem. Phys*. 5, 5472-5476 (2003).

27 Zhou, W.; Vavro, J.; Nemes, N. M.; Fischer, J. E.; Borondics, F.; Kamarás, K.; Tanner, D. B. Charge Transfer and Fermi Level Shift in p-Doped Single-Walled Carbon Nanotubes. *Phys. Rev. B* 71, 205423 (2005).

28 Blauwe, K. D.; Kramberger, C.; Plank, W.; Kataura, H.; Pichler, T. Raman Response of $FeCl_3$ Intercalated Single-Wall Carbon Nanotubes at High Doping. *Phys. Status Solidi B* 246, 2732 (2009).

29 Kim, S. M.; Kim, K. K.; Jo, Y. W.; Park, M. H.; Chae, S. J.; Duong, D. L.; Yang, C. W.; Kong, J.; Lee, Y. H. Role of Anions in the $AuCl_3$-Doping of Carbon Nanotubes. *ACS Nano* 5, 1236–1242 (2011).

30 Greiner, M. T.; Helander, M. G.; Tang, W. M.; Wang, Z. B.; Qiu, J.; Lu, Z. H. Universal Energy-Level Alignment of Molecules on Metal Oxides. Nat. Mat. 11, 76–81 (2012).

31 Aravinda, L.S.; Nagaraja, K.K.; Udaya Bhat, K.; Bhat, B. R. Magnetron Sputtered MoO_3/Carbon Nanotube Composite Electrodes for Electrochemical Supercapacitor. *J. Electroanal. Chem*. 699, 28 (2013).

32 Mahmood, Q.; Yun, H. J.; Kim, W. S.; Park H. S. Highly Uniform Deposition of MoO_3 Nanodots on Multiwalled Carbon Nanotubes for Improved Performance of Supercapacitors. *J. Power Sources* 235, 187 (2013).

33 Ni, J.; Wang, G.; Yang, J.; Gao, D.; Chen, J.; Gao, L.; Li, Y. Carbon Nanotube-Wired and Oxygen-Deficient MoO_3 Nanobelts with Enhanced Lithium-Storage Capability. *J. Power Sources* 247, 90 (2014).

34 De, S.; Coleman J. N. Are There Fundamental Limitations on the Sheet Resistance and Transmittance of Thin Graphene Films? *ACS Nano* 4, 2713–2720 (2010).
35 D'Arsie, L.; Esconjauregui, S.; Weatherup, R.; Guo, Y.; Bhardwaj, S.; Centeno, A.; Zurutuza, A.; Cepek, C.; Robertson, J. Stability of Graphene Doping with MoO_3 and I_2. *Appl. Phys. Lett*. 105, 103103 (2014).
36 Wu, Q-H.; Zhao, Y.; Hong, G.; Ren, J-G.; Wang, C.; Zhang, W.; Lee, S-T. Electronic Structure of MoO3−x/Graphene Interface. *Carbon* 65, 46 (2013).
37 Chen, Z.; Santoso, I.; Wang, R.; Xie, L. F.; Mao, H. Y.; Huang, H.; Wang, Y. Z.; Gao, X. Y.; Chen, Z. K.; Ma, D.; et al. Surface Transfer Hole Doping of Epitaxial Graphene Using MoO_3 Thin Film. *Appl. Phys. Lett*. 96, 213104 (2010).
38 Han, C.; Lin, J.; Xiang, D.; Wang, C.; Wang, L.; Chen, W.; Improving Chemical Vapor Deposition Graphene Conductivity Using Molybdenum Trioxide: an *in-situ* Field Effect Transistor Study. *Appl. Phys. Lett*. 103, 263117 (2013).
39 Han, C.; Xiang, D.; Zheng, M.; Lin, J.; Zhong, J.; Sow, C. H.; Chen, W. Tuning the Electronic Properties of ZnO Nanowire Field Effect Transistors *via* Surface Functionalization. *Nanotechnology* 26, 095202 (2015).
40 Xiang, D.; Han, C.; Wu, J.; Zhong, S.; Liu, Y.; Lin, J.; Zhang, X-A.; Hu, W. P.; Özyilmaz, B.; Castro Neto, A. H.; *et al*. Surface Transfer Doping Induced Effective Modulation on Ambipolar Characteristics of Few-Layer Black Phosphorus. *Nat. Commun*. 6, 6485 (2015).
41 Vasilopoulou, M.; Douvas, A. M.; Georgiadou, D. G.; Palilis, L. C.; Kennou , S.; Sygellou, L.; Soultati, A.; Kostis, I.; Papadimitropoulos, G.; Davazoglou, D. *et al*. The Influence of Hydrogenation and Oxygen Vacancies on Molybdenum Oxides Work Function and Gap States for Application in Organic Optoelectronics. *J. Am. Chem. Soc*. 134, 16178 (2012).
42 Futaba, D. N.; Hata, K.; Yamada, T.; Hiraoka, T.; Hayamizu, Y.; Kakudate, Y.; Tanaike, O.; Hatori, H.; Yumura, M.; Iijima, S. Shape-Engineerable and Highly-Dense Packed Single-Walled Carbon Nanotubes and Their Application as Super-Capacitor Electrodes *Nat. Mater*. 5, 987– 994 (2006).
43 Chakrapani, N.; Wei, B.; Carrillo, A.; Ajayan, P. M.; Kane, R. S. Capillarity-Driven Assembly of Two-Dimensional Cellular Carbon Nanotube Foams Proc. Natl. Acad. Sci. U.S.A. 101, 4009– 4012 (2004).

44 Xu, M.; Futaba, D. N.; Yumura, M.; Hata, K. Alignment Control of Carbon Nanotube Forest from Random to Nearly Perfectly Aligned by Utilizing the Crowding Effect. ACS Nano 6, 5837-5844 (2012).
45 Krishnan, K. S.; Ganguli, N. Large Anisotropy of the Electrical Conductivity of Graphite. Nature 144, 667-667 (1939).
46 Cho, Y. C.; Lee, S.; Ajmal, M.; Kim, W. K.; Cho, C. R.; Jeong, S. Y.; Park, J. H.; Park, S. E.; Park, S.; Pak, H. K. *et al*. Copper Better than Silver: Electrical Resistivity of the Grain-Free Single-Crystal Copper Wire. Cryst. Growth Des. 10, 2780–2784 (2010).
47 Guo, Y.; Robertson J. Origin of the High Work Function and High Conductivity of MoO_3. Appl. Phys. Lett. 105, 222110 (2014).
48 Delaney, P.; Choi, H. J.; Ihm, J.; Louie, S. G.; Cohen, M. L. Broken Symmetry and Pseudogaps in Ropes of Carbon Nanotubes. *Nature* 391, 466-468 (1998).
49 Zhou, W.; Vavro, J.; Nemes, N.; Fischer, J. Charge Transfer and Fermi Level Shift in p-Doped Single-Walled Carbon Nanotubes. Phys. Rev. B 71, 205423 (2005).
50 Woodruff, D. P.; Delchar, T. A. Modern Techniques of Surface Science (Cambridge University, Cambridge, 1994).